Estuarine, Coastal and Shelf Science 309 (2024) 108942

Contents lists available at ScienceDirect

Estuarine, Coastal and Shelf Science

journal homepage: www.elsevier.com/locate/ecss

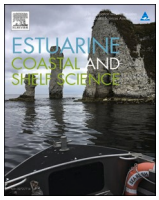

Long-term observations of the turbid outflow plume from the Russian River, California

William H. Speiser [a,b,*], John L. Largier [a,b,c]

[a] Hydrologic Sciences Graduate Group, University of California Davis, Davis, USA
[b] Bodega Marine Laboratory, Coastal and Marine Sciences Institute, University of California Davis, Bodega Bay, USA
[c] Department of Environmental Science and Policy, University of California Davis, Davis, USA

ARTICLE INFO

Keywords:
MODIS
Nearshore oceanography
River plumes
Turbidity
Small Mountainous River System
Wind forcing

ABSTRACT

Understanding the mechanisms that spread freshwater away from small river systems and form turbid, low-salinity coastal plumes is crucial for assessing water quality in coastal waters. We present an analysis of 15 years (January 2004 to December 2018) of daily MODIS Aqua satellite data and in situ instrument data on the turbid freshwater plume that forms off the Russian River (California, USA), a prototypical Mediterranean-climate, small mountainous river system (SMRS). We present per-pixel statistical metrics and regression analyses to identify and quantify the controls on the extent and configuration of the plume exerted by river discharge, waves, winds, and tides. While freshwater outflow exhibits a persistent signal in nearshore waters, a large-scale plume only extends offshore into coastal waters during high river flow, when plume turbidity can be detected more than 10 km offshore from the river mouth. Our results show times when wave radiation stress exceeds outflow inertia, confining the plume within the surf zone and leading to an absence of detectable plume turbidity in coastal waters. Although tidal currents significantly influence the plume near the inlet, wind forcing is the primary control on plume shape and extent in coastal waters, deflecting the turbid outflow more than 30 km upcoast or downcoast of the river mouth with respective wind directions. Coriolis forcing is also significant and observed most clearly during periods of high river discharge and low wind forcing. In addition to introducing novel remote sensing methodology for SMRS plume analyses, these findings highlight the complex interplay of forcing related to tides, river discharge, winds, and waves in shaping the behavior of SMRS plumes. New insights include the impact of tides on larger discharges, the role of Coriolis forcing in SMRS plumes, and the effect of cross-shore winds on plume compression. Further, by considering the Russian River as a model for SMRS, this study can be used to ground-truth existing numerical models of small river plumes and to contribute to understanding critical for managing coastal water quality and nearshore ecosystems.

1. Introduction

In coastal regions with dry summers and wet winters, outflow from small mountain river systems (SMRS) significantly influences the biogeochemical and geomorphic balances in coastal waters (Wheatcroft et al., 2010). These river systems (e.g. Russian, Gualala, Garcia, Navarro, Big, Noyo, Ten Mile, and Mattole Rivers in Northern California, USA) are characterized by small river basins ($<2 \times 10^4$ km^2) and high relief (>1000m). Outflow fluctuates between near-zero summer discharges (order 1 m^{3}s^{-1}) and winter discharges several orders of magnitude higher (order 1000 m^{3}s^{-1}), transporting seasonal concentrations of sediments to the coastal ocean, exacerbated by interannual drought and flood cycles (Wheatcroft et al., 2010).

In Mediterranean-climate regions like Northern California, sediments from these outflows supply over 80% of the sediment to littoral cells (Griggs and Hein, 1980; Runyan and Griggs, 2003). Coarse sediments in these outflows deposit quickly nearshore, contributing to the cycle of shoreline morphodynamics (Warrick, 2020). Finer sediments remain suspended in a surface freshwater layer (or plume) that can travel hundreds of kilometers alongshore (Warrick et al., 2007). These suspended particles increase water turbidity, affecting both light attenuation through the water column and acting as a tracer for sorbed riverine pollutants.

Despite the significant role of SMRS outflow, most research has

* Corresponding author. 5975 Keith Ave Apt 2, Oakland, CA, 94618, USA.
E-mail address: whspeiser@ucdavis.edu (W.H. Speiser).

https://doi.org/10.1016/j.ecss.2024.108942
Received 9 January 2024; Received in revised form 27 June 2024; Accepted 9 September 2024
Available online 10 September 2024

focused on larger river systems and small constructed engineered outflows (see discussions in Basdurak et al., 2020). This research gap is important because SMRS differ significantly from these systems in terms of discharge and plume dynamics. SMRS have lower average discharges than larger rivers, making their plume trajectories more dependent on variable environmental forcings rather than the classical, constant buoyancy-rotation balance (Horner-Devine et al., 2015). At the same time, SMRS outflows are more stratified and less dependent on jet dynamics compared to engineered outflows (Basdurak et al., 2020). SMRS discharges also vary significantly, reflecting values that fall between those of larger river systems and engineered outflows.

Recent studies have begun addressing plumes from SMRS, primarily using computational models, with few utilizing remote sensing or in situ observations. Remote sensing and observational research are crucial for validating the results of computational models, (see section 1.1). Remote sensing studies typically use the light reflectivity of coastal waters as a proxy for the concentration of suspended particles in river plumes. These studies can be broadly categorized based on the spatial and temporal resolution of remotely sensed data. High spatial resolution studies make use of imagery from Unmanned Aerial Vehicles (UAVs) and fine-resolution satellites like Landsat 5–9 and Sentinel 2. However, these studies are often limited in temporal scope due to the logistical challenges of UAV sampling and the infrequent repeat overpasses of high-resolution satellites. In contrast, low spatial resolution sensors (e.g., SeaWIFS, MODIS) benefit from more frequent data but lack fine-scale spatial resolution and prior works tend to focus on statistical metrics like mean and standard deviation rather than more nuanced statistical tests such as correlation and regression, thus overlooking the variability common in small plumes. Moreover, much of this work predates recent findings on the significant impacts of waves (Rodriguez et al., 2018; Kastner et al., 2019) and tides (Basdurak et al., 2020) on smaller plumes. Computational studies often focus on a specific mechanism, thus precluding a more holistic view of plume dispersion mechanics.

This study aims to enrich understanding of SMRS plume dispersion by observing turbid outflow from the Russian River in northern California (USA), with a prototypical, seasonally variable hydrograph. We validate and enrich numerical models across river plume literature by using updated techniques to compare nearly two decades of remote sensing data from MODIS with coincident data on waves, tides, and river discharge. Our geospatial results not only align with existing models across various plume sizes but also reveal previously unexplored controls on plume shape and the fate of freshwater outflow. We show that the seasonality of discharge in the Russian River SMRS results in plumes that exhibit behaviors consistent with "small" plumes during low flows (plume controlled by wave and wind conditions) and "large" plumes during high flows (plume controlled by buoyancy and Coriolis effects).

Our primary objectives are (i) to identify and quantify the spatial configuration of small river plumes subject to wind, wave and tidal forcing, (ii) to develop and deploy new methodologies in river plume remote sensing (iii) to validate and enrich prior simulation models of plumes, and (iv) to contrast controls on "large" Coriolis-influenced plumes to controls on "small" river plumes.

1.1. River plumes

River plumes are bodies of freshwater that flow from a river into another body of water, such as lakes or the ocean. When entering marine waters, these plumes often form a relatively thin layer of freshwater that is stratified at the surface due to its higher buoyancy compared to denser, saline ocean water (Horner-Devine et al., 2015). Large and small plumes are often delineated by the degree to which the trajectory of their dispersion is dependent on rotational Coriolis forces (Horner-Devine et al., 2015; Basdurak et al., 2020). This relationship is explored by Garvine (1995), where large and small plumes are classified by a non-dimensional Kelvin number K:

$$K = \frac{\gamma L}{(c/f)} \quad \text{eq. 1}$$

Where γ is plume thickness, L is the alongshore length of the plume, c is the internal wave phase speed, and f is the coriolis parameter. "Large" plumes occur where Coriolis is dominant ($K \gg 1$) and "small" plumes occur where Coriolis effects are dominated by inertia and buoyancy effects ($K \ll 1$). Typical large-plume patterns and outflow trajectories are well documented (Horner-Devine et al., 2015). As the low-density outflow leaves the outlet, it enters the near-field plume region where transport is driven by outflow momentum. Eventually, the plume lifts from the seabed at the critical Froude number (Armi and Farmer, 1986) marking the mid-field region, where dispersion of the buoyant plume layer is shaped by an interplay between buoyancy (Hetland, 2010), wind (Rennie et al., 1999; Lentz and Largier, 2006; Horner-Devine et al., 2009), Coriolis (Horner-Devine et al., 2015), and discharge (Fong and Geyer, 2002; Horner-Devine et al., 2009). The influence of Coriolis results in an anti-cyclonically rotating "bulge", which scales in size with discharge rate and duration (Horner-Devine et al., 2009). Beyond the bulge is the far-field where transport is no longer controlled by discharge and the buoyant plume layer travels alongshore as a shore-attached coastal buoyancy current. Both the mid- and far-field regions of the plume can be impacted by winds and currents. Upwelling increases the extent of the bulge and induces thinning in the plume; downwelling winds cause opposite effects (Fong and Geyer, 2001; Lentz and Largier, 2006; Horner-Devine et al., 2009). While sufficiently strong winds can overcome Coriolis effects in large plumes (Pullen and Allen, 2001; Horner-Devine et al., 2009), this is more common in small plumes ($K \ll 1$) that are less susceptible to Coriolis effects (Basdurak et al., 2020; Basdurak and Largier, 2022).

Some recent publications highlight the role of wave forcing (Wong et al., 2013; Rodriguez et al., 2018; Kastner et al., 2019). Depending on the balance between estuary outflow, tidal influences, and breaking wave momentum, river water can be partially or fully trapped in the surf zone. Rodriguez et al. (2018) model the balance of momentum (p) between breaking waves and river discharge with the following equation:

$$\frac{S_{xx}^{b}}{\rho_0 \beta L_{sz}} \frac{A^2}{Q^2} = p \quad \text{eq. 2}$$

where Q is river discharge, S_{xx}^{b} is wave radiation stress, βL_{sz} is the water depth at the breaking point, ρ_0 is the background density of ocean water, and A is the cross-sectional area at the river or estuary mouth. As p increases, more freshwater is trapped in the surf zone. Given a high enough value of p, river outflow becomes completely trapped and is transported alongshore in the surf zone until later dispersed offshore by rip currents (Clarke and Largier, 2007).

When outflow momentum dominates and river water escapes the surf zone, dispersion pathways can still be influenced by waves and tides. Basdurak et al. (2020) show that small plumes are deflected up and down coast from the estuary mouth by alongshore tidal currents. Other works model the role of wave breaking in turbulent mixing that can slow near-field advection and far-field dispersion (Gerbi et al., 2013; Thomson et al., 2014).

1.2. Site description

This study focuses on outflow from the Russian River (California, USA) a prototypical small mountainous river system (SMRS) in northern California (Fig. 1) that is representative of outflows from mountainous coasts worldwide. The mouth of the river is about 90 km north of San Francisco, and the 180-km long river drains a 3850 km^2 watershed subject to intense rainfall events in winter (i.e., atmospheric river events). Winds are seasonal, with persistent strong northerly winds driving coastal upwelling in spring and summer (April to June), southerly wind events during winter storms (December to February), and

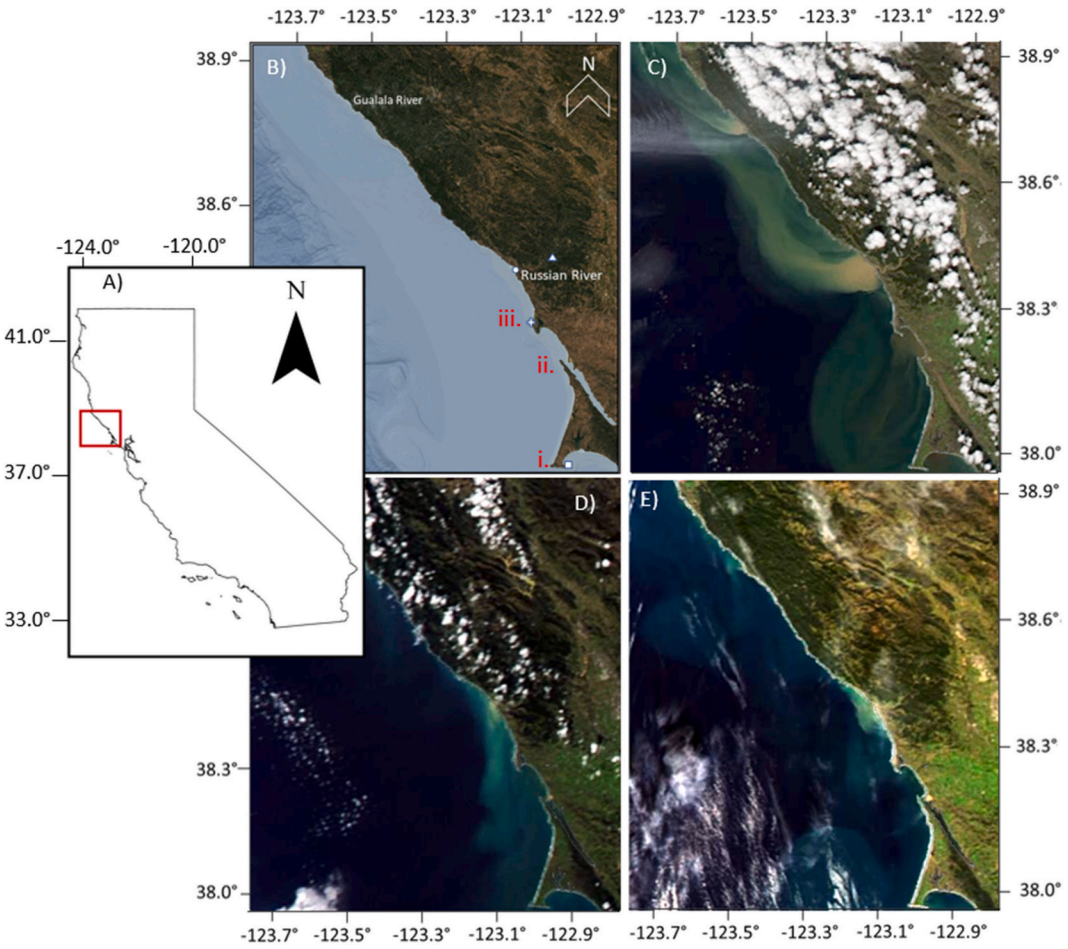

Fig. 1. (A) Map of California, USA, study site highlighted by red box (B) Map of study site and data sources (● = Russian River Inlet & CDIP MOP wave energy location, ▲ = USGS River Gauge #11467000, ✚ = BOON wind observatory, ■ = NOAA Tide Gauge Station #9415020). Roman numerals mark (i) Point Reyes, (ii) Bodega Bay and Tomales Bay, and (iii) Bodega Head. (C–E) Examples of turbid river plumes from MODIS true color images: (C) February 28, 2019, (D) February 28, 2017 and (E) February 28, 2008. (For interpretation of the references to color in this figure legend, the reader is referred to the Web version of this article.)

weaker winds in the fall (August to October) as described by Garcia-Reyes and Largier (2012).

At the mouth of the Russian River is a bar-built estuary that is intermittently closed off from the ocean by a wave-built sand barrier (Behrens et al., 2013). Adjacent to the mouth of the estuary, the shores are rocky, and waters are designated as a Marine Protected Area. During high precipitation events, river discharge exceeds 1000 m^3/s, but during low discharge conditions (~4 m^3/s) water enters and exits the estuary mouth tidally. Comparable conditions exist in many other northern California estuaries.

2. Methods

This study uses daily satellite data and concurrent data on river flow and environmental conditions. Data on river discharge (Q), wind (W), ocean water level (WL), river turbidity (T), and wave height (Hs) are available from 2004 to 2019. Environmental data are binned in intervals preceding each satellite overpass: W, T, Q, and Hs are averaged over the preceding 24 h while WL is averaged hourly.

2.1. Environmental data

Winds: Wind direction and magnitude at Bodega Head were observed with a 4-blade helicoid propeller and wind vane from May 2001 to May 2014, and with a 2-axis ultrasonic anemometer after May 2014 (BOON; https://boon.ucdavis.edu/). Daily wind direction was classified in quadrants relative to the shoreline orientation of 315°: winds blowing from directions between 90° and 180° are classed as "upcoast", between 0° and 90° as "off-coast", between 270° and 360° as "downcoast", and between 180° and 270° as "on-coast". The daily alongshore wind component is calculated from daily wind speed and direction at an orientation of 315° (i.e., downcoast winds have positive magnitudes) and the cross-shore wind component is calculated for an orientation of 225° (i.e., on-coast winds have positive magnitudes). Wind data were averaged for the 24 h prior to the satellite overpass (zero lag), or for 27-3 h prior (3-hr lag), or for 30-6 h prior (6-hr lag). Correlations with greater lag have previously been found to yield stronger relations between plume behavior and wind stress (Geyer et al., 2000; Warrick et al., 2007).

Tides: Water level data were used to index tidal phase at the time of each satellite image. Data referenced to MLLW were obtained from the tide gage at Point Reyes (National Oceanic and Atmospheric Administration gage #9415020), which is known to represent tides at the Russian River mouth with negligible phase and amplitude differences (J. L. Largier and D.S. Behrens unpublished data). Water level data are hourly averaged and matched with the time of image capture time rounded to the nearest hour.

River Discharge and Turbidity: Russian River discharge and turbidity data were collected at Hacienda Bridge (United States Geological Survey gauge #11467000), approximately 18.5 km upstream of the mouth. Quarter-hourly discharge values are available from October 1987 onward, and turbidity data are available since June 2008. Turbidity is

measured in FNU units with a monochrome near-infrared LED light (780–900 nm) at a detection angle of 90° ± 2.5°.

Waves: Daily average significant wave height H_s at the 10m isobath adjacent to the Russian River mouth (Fig. 1) are available from the Coastal Data Information Program (CDIP; https://cdip.ucsd.edu/). These values are generated using a linear, spectral refraction wave model driven by observations at offshore wave buoys (O'Reilly et al., 2016). Radiation stress (S_x^b) is calculated by assuming that phase velocity equals the group velocity in shallow nearshore waters:

$$S_{xx}{}^b = E = \rho_0\, g\, H_s{}^2 \qquad \text{eq. 3}$$

where E is the mean-depth wave energy density per unit horizontal area and g is gravitational acceleration.

Daily average S_{xx}^b and Q were used to calculate a daily value of p (Eqn (2)). The value of βL_{sz} is approximated by depth d. This depth is estimated using the theoretical equation from Miche (1944) where the depth-limited breaking of a solitary wave occurs at a critical value of $H_s/d = 0.781$ (Kastner et al., 2019). The cross sectional-area (A) is assumed to be 100 m^2, consistent with the average dimensions of the inlet channel at the Russian River mouth (Behrens et al., 2013).

Mouth State: Daily observations of the state of the Russian River mouth are available from 2004 to 2019, allowing classification as open or closed (Behrens, 2013; Largier et al., 2020; Winter 2020). These data were extracted from a daily photograph record.

2.2. Satellite data

Ocean color data were collated for every MODIS Aqua image captured for the study region (38.95°- 37.99°N, 123.75°–122.85° S) between January 2004 and December 2018, aligning with daily Russian River inlet-state data. Daily MODIS L1A files were downloaded from NASA's Ocean Color website (http://oceancolor.gsfc.nasa.gov/) and subsequently processed to L1B and L2 surface reflectance data (*Rrs*) using the SeaDas (SeaWIFS Data Analysis System, version 8.1.0, Baith et al., 2001).

Atmospheric correction was performed using the NIR-SWIR (Near Infrared Radiation-Shortwave Infrared Radiation) algorithm by Wang et al. (2009). Traditional atmospheric correction methods rely solely on NIR bands (748 and 869 nm), but these are not suitable for turbid water conditions. Hence, the Wang et al. (2009) method switches from NIR to SWIR (1240 and 2130 nm) correction for pixels detected as turbid by an index (Wang et al., 2009; Saldias et al., 2012). We used a pixel size of 500m rather than 250m to resolve heterogeneity in imagery pixels that arise from issues such as sun glint (Aurin et al., 2013).

Surface reflectance from the 645 nm band (Rrs_{645}) is an accepted proxy for surface turbidity due to suspended sediments, based on correlations in prior studies (e.g., Lahet and Stramski, 2010; Saldias et al., 2016). We validate this relation for our study site by finding the Spearman non-linear correlation coefficient between Rrs_{645} and hourly average turbidity measured at the Hacienda Bridge gage, 18.5 km from the river mouth. We do this independently for each pixel for an image time series from June 2008 to January 2019. Spearman Rho values are 0.8 at the mouth, demonstrating that reflectance is an effective turbidity metric, and above 0.7 for locations up to 4.5 km offshore of the mouth (Fig. 2), despite the spatial offset and potential for changes in turbidity between the river gauge and pixels in coastal waters.

2.3. Plume detection

To isolate river plume effects on ocean turbidity apart from other processes (e.g., phytoplankton blooms, wave-driven resuspension, rip currents, white capping), we examine the distribution of turbidity values in coastal waters on dates when the river inlet was observed as closed. We determined a threshold value of 0.59×10^{-3} Sr^{-1} for non-plume turbidity by calculating the 97th percentile value of Rrs_{645} values for all pixels 1.5 km offshore across 1371 images captured when the Russian River inlet was closed (Fig. 3). This threshold assumes that in the absence of sediment-laden freshwater, the ambient Rrs_{645} reflectance of oceanic waters is much less than reflectance values associated with the plume. Therefore, the maximum non-freshened values would represent the highest condition before Rrs_{645} is elevated by freshwater sediment influence. The 3% of values exceeding this threshold are likely due to occasional wave-driven events that cause resuspension and circulation, exporting nearshore turbidity offshore (Speiser et al., in preparation). Nonetheless, even these high values rarely exceed 1.0×10^{-3} Sr^{-1}, which is an order of magnitude lower than typical plume turbidity values (Fig. 4). Similar thresholding methodologies have been applied in other river plume remote sensing studies, although without the advantage of an estuary closure (for example, Saldias et al., 2012; Mendes

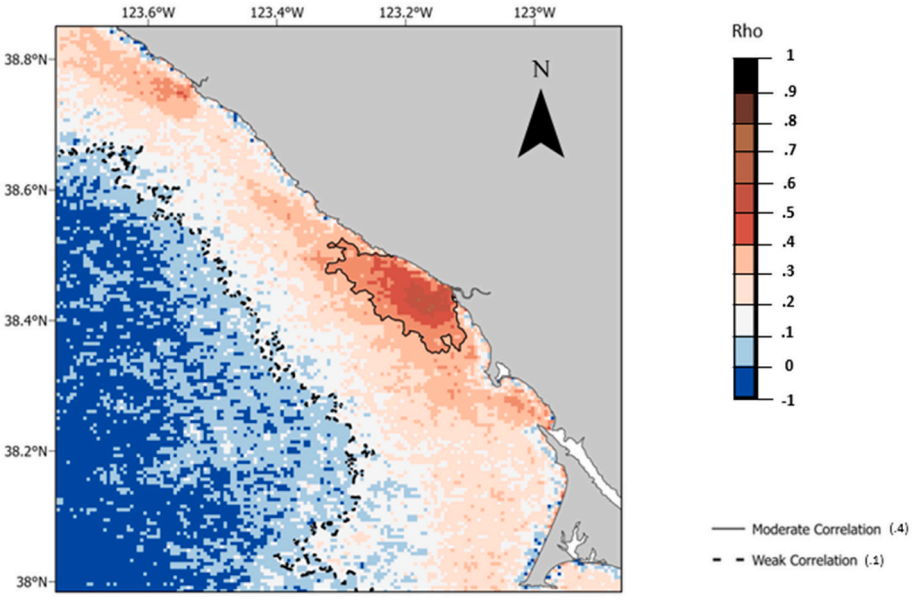

Fig. 2. Map of pixel-wise Spearman's rho correlation coefficients between hourly-average measured turbidity from USGS gauge #11467000 and coincident Rrs_{645} at each pixel position.

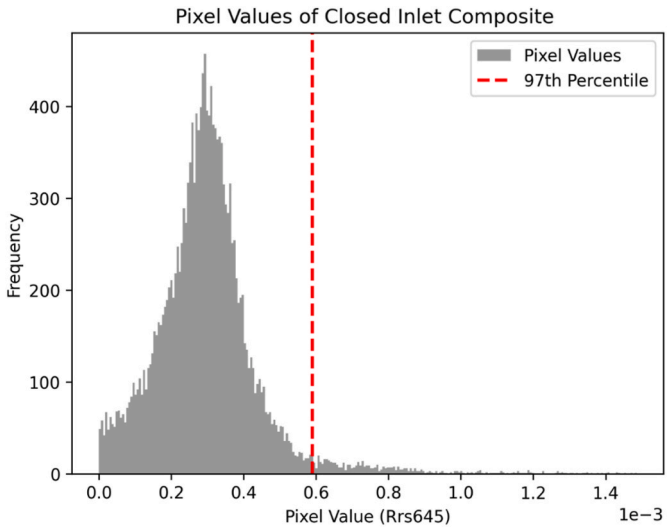

Fig. 3. Frequency histogram of the average Rrs_{645} at all pixels 1.5 km offshore from all MODIS images on days when the Russian River mouth was closed. The red line marks the 97th percentile value, 0.59×10^{-3} Sr^{-1}. (For interpretation of the references to color in this figure legend, the reader is referred to the Web version of this article.)

et al., 2014; Saldias et al., 2016).

2.4. Regression analysis

To evaluate the influence of different environmental drivers on plume behavior we calculated Spearman's Rho non-linear regression correlation coefficients between coincident environmental data (i.e., *W, Hs, WL, Q*, and *T*) and turbidity proxy values Rrs_{645} at each pixel position across the study region. We used statistical tests (pixel correlations) instead of pixel mean or median to differentiate between different processes that occur simultaneously. Further, by evaluating per-pixel regression we can identify spatial patterns in processes controlling plume presence. Spearman's rho ordinal rank correlation was chosen over linear regression as pixel values are altered simultaneously by other drivers and Spearman does not require linear relationships. For instance, the turbidity of a pixel may be strongly influenced by river discharge, but transport to that specific position may be diminished or enhanced by processes such as wind-driven transport, altering the pixel Rrs_{645} value. Further, Spearman's rho correlation coefficients are less impacted by outliers, which are caused by non-observed variables, thus highlighting relationships with the tested variable.

To assess the strength of correlation we adopt the classes outlined by Schober et al. (2018) – Table 1. To demarcate spatial extent of the correlation, contours are drawn to encompass the mouth of the Russian River. If a contour does not surround the river inlet, it is not highlighted. The value ranges for these classes are determined to the second decimal (i.e., 0.394 falls in the "weak correlation class", while 0.395 is rounded to 0.40 and falls in the "moderate correlation" class). This approach precludes attention on features due to other river outflows or wave-driven rip-current features.

3. Results

3.1. Nearshore trapping of plume

As found by Rodriguez et al. (2018), wave radiation stress can stall or fully trap the outflow jet, precluding the formation of a plume beyond the nearshore (surf zone and rip-current zone), which is the focus of this paper. Thus, instead of using a minimum daily average discharge as a qualifier for images used in plume analyses (e.g. Saldias et al., 2012; Mendes et al., 2014; Fernandez-Novoa et al., 2015; Saldias et al., 2016), we use a qualifying threshold based on daily average *p* value. For all images when the Russian River inlet was open (n = 3419), we calculated the daily average *p* and divided the dataset into deciles. For each decile, we created an average image. Only the lowest four p-value deciles exhibit reflectance values 1 km offshore that exceed the plume turbidity threshold. The 1 km location was chosen to mitigate any influence of subpixel constituents such as land, boulders, and white water and foam lines generated by breaking waves. We thus use p = 41 as the upper bound for images used in our evaluation of the offshore turbid plume (a total of 1357 images). This is the lower bound of the 4th decile (not the average *p* value 109), i.e., only the three lowest deciles are used in the analysis. The distributions of available pixels across these images are mapped in Fig. 4., with an average of n = 498 values at each pixel position, a minimum of n = 27 and a maximum of n = 650.

Table 1
Correlation strength classes from Schober et al. (2018).

Absolute value of Rho	Interpretation
0.00–0.10	Negligible Correlation
0.10–0.39	Weak Correlation
0.40–0.69	Moderate Correlation
0.70–0.89	Strong Correlation
0.90–1.00	Very Strong Correlation

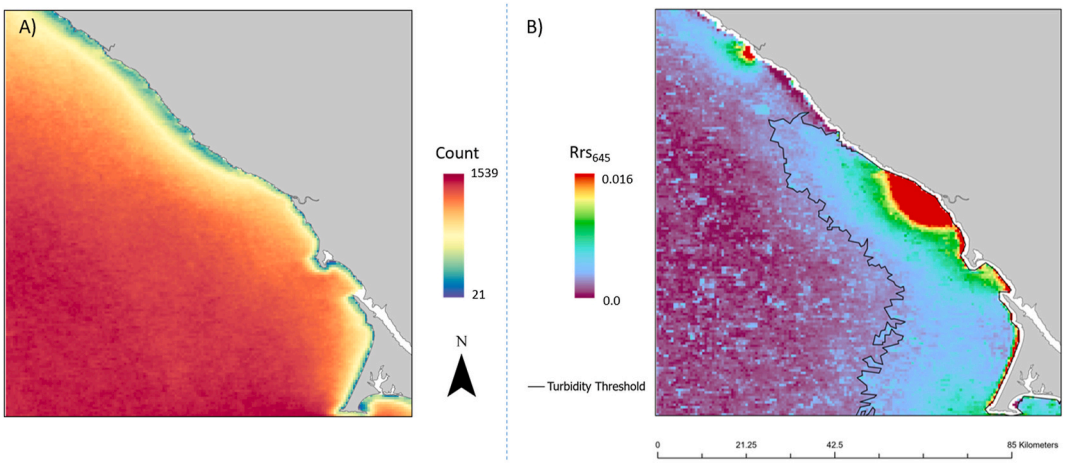

Fig. 4. Mapped statistics of dataset images when plume breaks through surf zone (A) Count of available values at each pixel position. (B) Pixel-wise average of Rrs_{645}, ranging from 0.0 to 0.016 Sr^{-1}. The black line is the contour where average Rrs_{645} equals plume turbidity threshold value of 0.59×10^{-3} Sr^{-1}.

3.2. Average plume pattern

The shape of the turbid plume exiting the Russian River can vary significantly (Fig. 1). However, there is a clear zone of elevated turbidity in the 1357-image average field that extends about 10 km upcoast, downcoast and offshore of the mouth (Fig. 4), encompassing the near-field and mid-field of most plume patterns. The far-field evidently varies across wind conditions with no clear pattern in the average. Further, other sources and processes are evident beyond 10 km, including outflow from the Gualala River (38.7° N), Tomales/Bodega Bay freshwater sources (38.2° N) and nearshore zones along wave-exposed beaches on the north shore of Bodega Head (38.3° N) and Point Reyes (38.1°N). The average alongshore (upcoast plus downcoast) extent of turbidity above the plume threshold increases with discharge rate, from 14 km for lowest discharge quintile to 54 km, 65 km, and 77 km for second through fourth quintiles, respectively. For the fifth discharge quintile, elevated turbidity from the Russian River merges with multiple sources in the region (cf., plume coalescence outlined by Warrick and Farnsworth, 2017). Average offshore extent is small for low discharge (3 km) but pushes significantly further offshore for higher discharge (8 km, 10 km, and 14 km for the second through fourth quintiles, respectively). The plume area encompassed by the turbidity threshold contour increases from 20 km^2 for low discharges to 180, 298, and 698 km^2 for second, third, and fourth quintiles respectively.

3.3. River discharge effects

As river outflow increases, a larger area of turbid water is observed in coastal waters off the Russian River mouth. This plume-affected zone is demarcated by high Spearman correlation values at pixels where Rrs_{645} turbidity increases with increases in river discharge Q. The spatial distribution of correlations mapped in Fig. 5 shows moderate correlations (greater than 0.4) in a zone extending 11 km offshore of the mouth and 30 km alongshore (darker colors enclosed by moderate correlation contour), both upcoast and downcoast of the mouth – but notably detached from the shoreline south of the mouth. The highest correlation (rho = 0.71) is about 4 km offshore of the Russian River mouth (Fig. 5) – lower correlations are found in persistently turbid nearshore waters. This core zone is strongly and predictably impacted by changes in river discharge, but there is an extensive zone of weaker correlations that is continuous through the study area from Point Reyes to Point Arena. The weak-correlation contour is found about 25 km offshore, indicating that discharge-related elevated turbidity extends over the entire shelf during times of high flow in the Russian River, although including multiple sources with correlated outflow following rain events.

Anticipating different plume behavior during high-discharge events and low-discharge events, pixel-wise turbidity-discharge correlations were calculated separately for each daily-average-discharge quartile (Fig. 6, panel d.). With highest river flow, the zone of moderate correlations is found primarily on the upcoast (north) side of the river mouth, pushing 18 km offshore, and separated from the coast. At the center of this zone, the maximum correlation is 0.83. While weak correlations extend over the whole shelf region, elevated correlations are observed in Bodega Bay where turbid outflows include Tomales Bay and Estero Americano (Fig. 1) and at the bottom of the frame where turbid waters flow north from the Gulf of Farallones (Largier et al., 1993; Kaplan and Largier, 2006; Largier et al., 2020). For plumes when discharge is in the second highest quartile (Fig. 6, panel c.), correlations are weaker but elevated values are again skewed to the upcoast side. The weak-correlation contour no longer extends over the shelf, and it is centered on the Russian River mouth, extending about 30 km upcoast and about 10 km downcoast separated from the coast. While a coherent zone of correlation is evident for the second lowest quartile (Fig. 6, panel b.) and weak correlations extend about 30 km alongshore and 15 km offshore, the correlation zone is notably weak for the lowest quartile discharge (Fig. 6, panel a.). While turbid plumes are observed on these low-discharge days, the shape and size of the plume is more variable, altered by tidal state (section 3.5) and wind forcing (section 3.4).

Wind forcing shows a correlation with discharge rate (Fig. 6), with more southerly winds during higher discharges and more northerly winds during lower discharges. To preclude the influence of wind on plume behavior, we also calculate pixel-wise correlation between Q and Rrs_{645} for calm days (wind speeds in the lowest quartile, which is less than 6.5 m/s). In the absence of strong wind effects (Fig. 7), correlations are higher (compare with Fig. 5), exhibiting a zone of strong correlation reaching 6 km offshore and 5 km upcoast. The maximum correlation

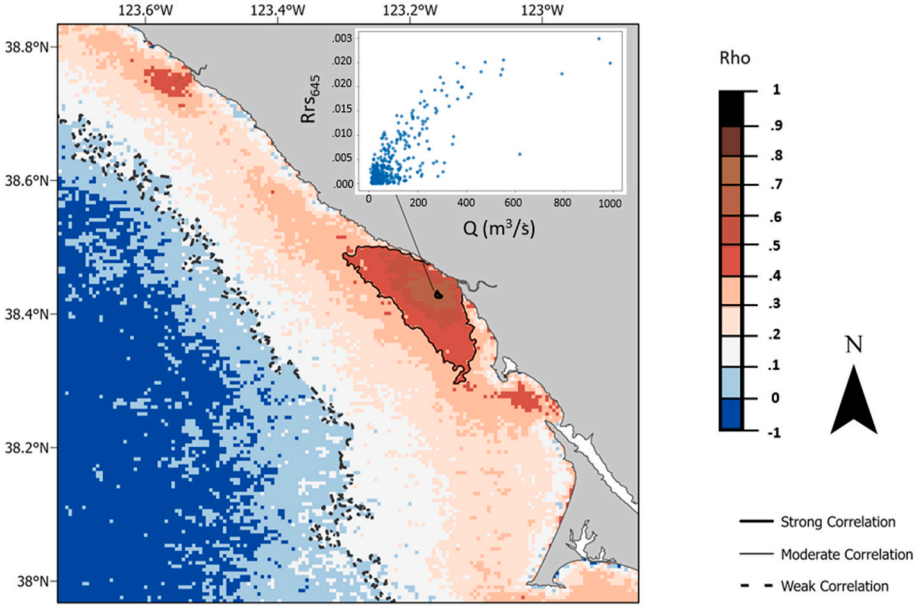

Fig. 5. Pixel-wise correlation coefficients between Rrs_{645} and coincident daily average discharge (Q) values for all dates with visible plumes (average Q is 156.52 m^3/s). The weak correlation (rho) threshold (rho = 0.10) and moderate correlation threshold (rho = 0.40) are shown; only a few pixels exceed the strong correlation threshold (rho = 0.70). The inset graph shows Rrs_{645} values (y axis) versus daily discharge values (x axis) for the pixel position with the highest correlation (rho = 0.71).

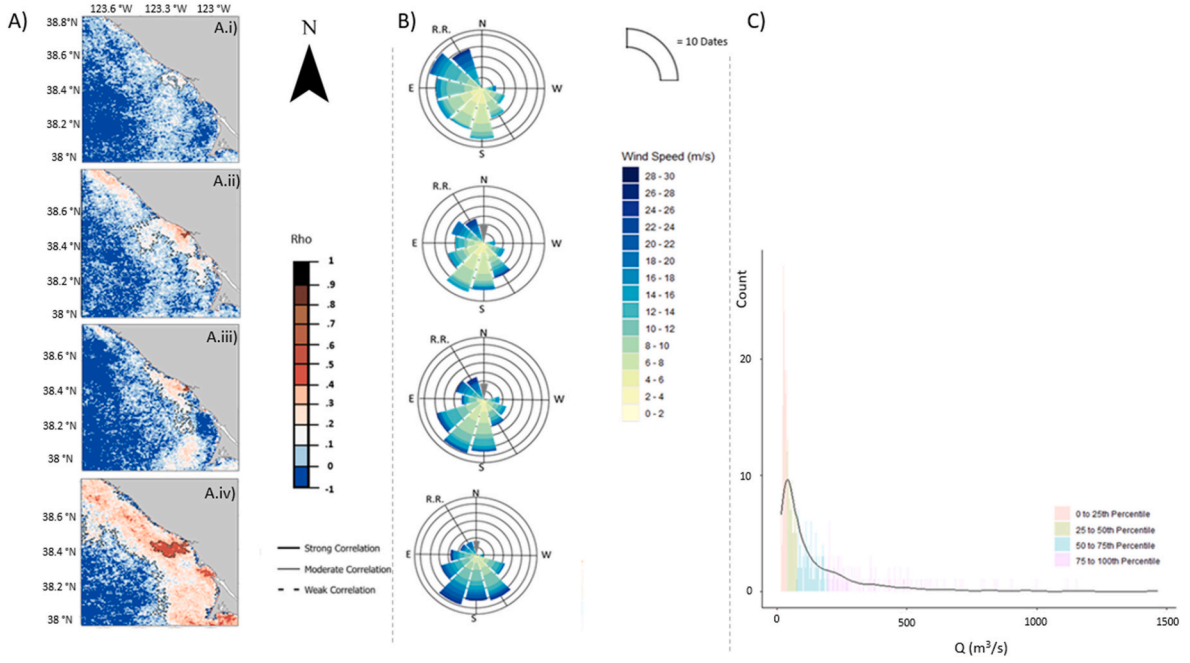

Fig. 6. (A) Pixel-wise correlation coefficients between Rrs_{645} and coincident daily average discharge (Q) values calculated separately for discharge quartiles from low to high (panels A. i-A.iv). (B) Wind roses corresponding to each quartile. The "RR" line indicates shoreline orientation at the mouth of the Russian River. Wind direction is in meteorological convention (i.e., direction from which the wind blows). (C) Histogram showing the discharge for each quartile; colors of bars correspond to respective discharge quartiles 0–25th percentile (16–42 m^3/s); 25th-50th percentile (42–84 m^3/s); 50th-75th (84–203 m^3/s); 75th to 100th percentile (203–2366 m^3/s). (For interpretation of the references to color in this figure legend, the reader is referred to the Web version of this article.)

coefficient is rho = 0.81. The moderate-correlation contour also exhibits marked asymmetry, extending ~20 km upcoast and ~5 km downcoast.

3.4. Wind effects

To explore wind effects on plume behavior we calculate discharge-turbidity relationships for different daily average wind direction (Fig. 8), and we calculate correlations between turbidity and wind speed in each of four quadrants (upcoast, downcoast, onshore, offshore) irrespective of discharge but with $p < 41$ as before (Fig. 9).

When the wind blows from the southeast (upcoast quadrant), turbidities increase markedly on the north side of the river mouth during high discharge, with a coherent band of strong correlation extending about 12 km upcoast from the mouth and separate from the shore.

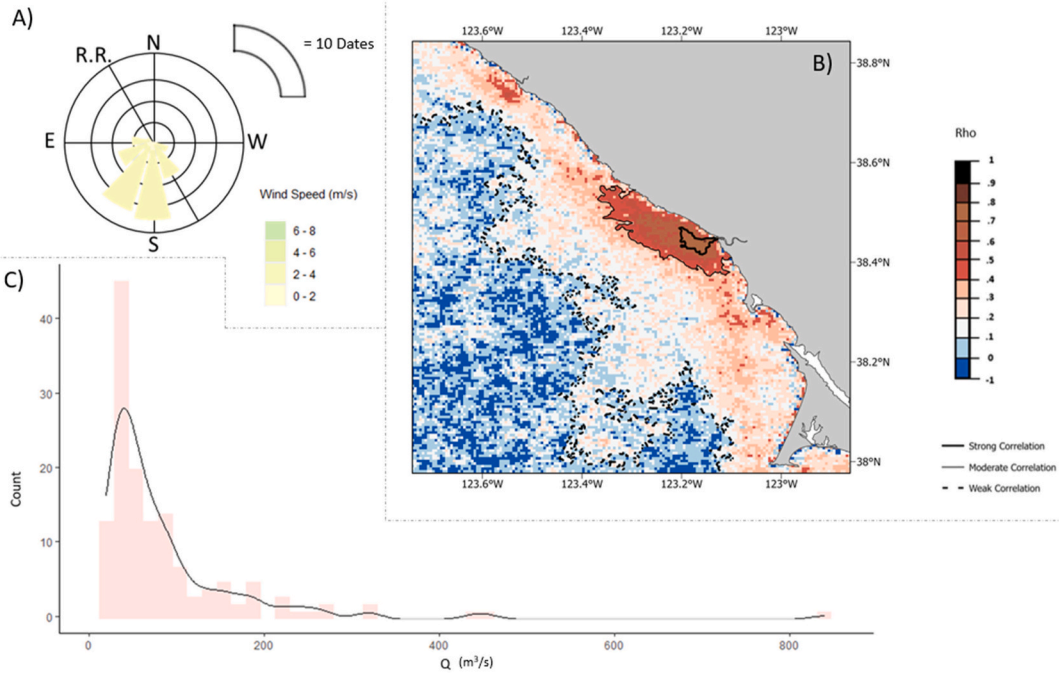

Fig. 7. (A) Pixel-wise correlation coefficients between Rrs_{645} and coincident daily average discharge (Q) values for days with weak winds. (B) Wind rose representing data from the subset, with wind direction in meteorological convention. (C) Histogram depicting discharge rates for this subset.

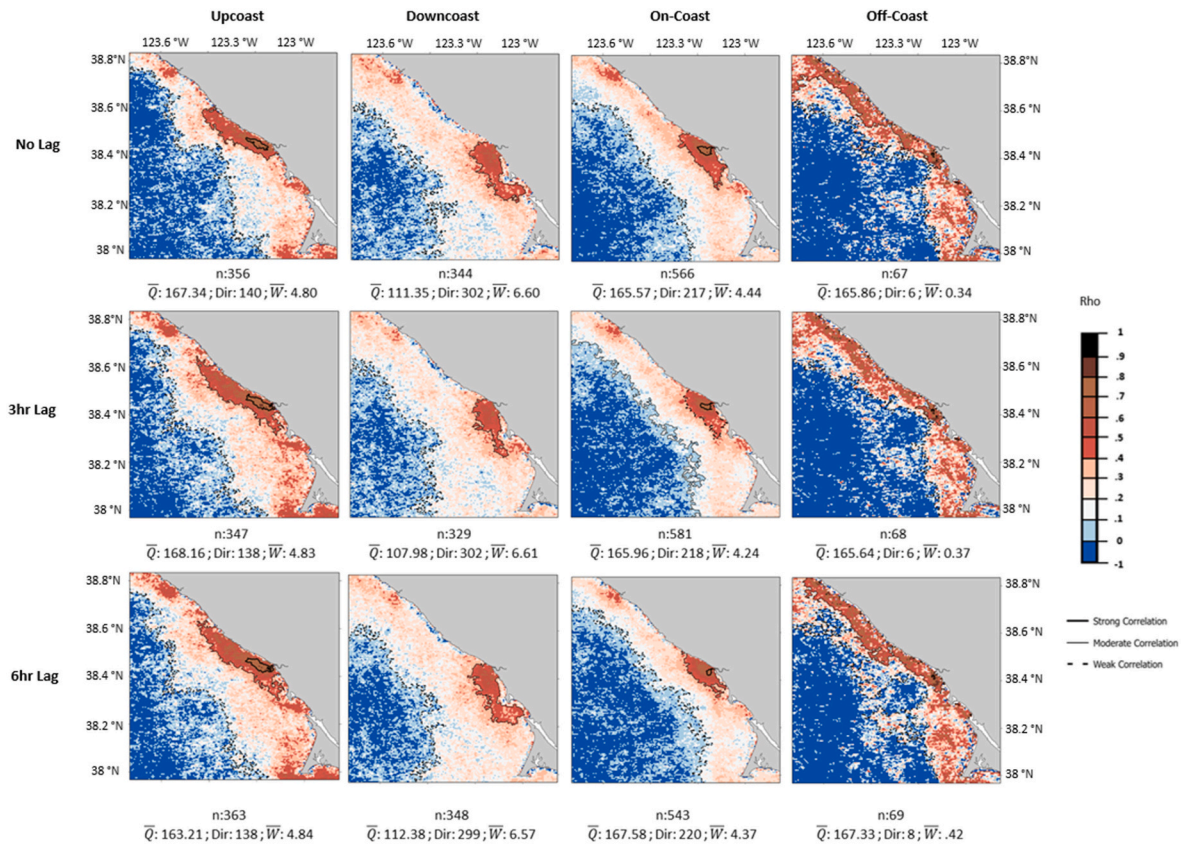

Fig. 8. Pixel-wise correlation coefficients between Rrs_{645} and coincident daily average Q values calculated separately for different wind directions (columns) and time lags (rows). The number of images in each subset (n) is listed beneath each image, along with information on average discharge (Q in m^3/s), average wind direction (Dir), and average wind speed in the subset (W in m/s). Columns, left to right: Daily average upcoast winds, downcoast winds, onshore winds, and offshore winds; Rows, top to bottom: no lag, 3 h lag, 6 h lag.

However, the broader zone of moderate correlation is attached to the shore and extends over 30 km upcoast (Fig. 8). When daily average discharge is shifted 3 h earlier (i.e., discharge averaged from 27 h to 3 h before the satellite image), or 6 h earlier, maximum correlations are similar, but the zone of moderate correlation extends further upcoast, increasing from 33 to 39 km consistent with an upcoast propagation rate of 0.28 m/s. Under these upcoast winds, significant discharge-turbidity correlations are also seen emerging from Bodega Bay sources and extending north from the Gulf of Farallones where outflow from San Francisco Bay enters the ocean – these turbidity signals also reach further north with increased lag between discharge and turbidity. In contrast, when the wind blows from the northwest (downcoast quadrant), turbidities increase markedly on the south side of the river mouth, although no pixels exhibit strong correlation. The 30 km zone of moderate correlation extends to Bodega Bay, but remains detached from the shore, consistent with active upwelling driven by NW wind stress and persistent nearshore turbidity along the north shore of Bodega Head. It is interesting to see this zone extending into Bodega Bay, most likely due to merging with turbidity from sources in Bodega Bay and Tomales Bay (cf., Fig. 1). The absence of discharge-correlated turbidity north of the mouth during NW winds shows that the upcoast configuration of the plume requires high discharge (Fig. 6) and/or weak winds (Fig. 7) – conditions under which Coriolis forcing is expected to be important.

Onshore and offshore winds also influence the shape of the plume (Fig. 8). During onshore winds (on-coast), only pixels near the mouth exhibit moderate or strong correlations, illustrating compression of the plume on the shore and limited alongshore plume propagation. Further, in contrast to the no-wind case (Fig. 7) there is no upcoast tendency. With increasing lag between discharge and turbidity, the moderate-correlation plume zone is further reduced in offshore extent, decreasing from 12 to 9 and 8.5 km, respectively. At the same time, the shelf-wide weak correlations are compressed from 32 to 14 and 12 km, respectively. In contrast, offshore winds (off-coast) result in a continuous band of high discharge-turbidity correlations along the coast, although there is notable small-scale spatial heterogeneity with adjacent pixels exhibiting different values.

The second analysis of wind influences on the plume addresses the correlation between turbidity at a given pixel and wind speed – calculated separately for four wind vector directions: upcoast, downcoast, onshore, and offshore. While discharge is not a factor, all data are from days when discharge is significant (i.e., the plume is not trapped in the surf zone, $p < 41$). Again, we calculate correlations for wind averaged over the day preceding the satellite overpass, and for daily average wind shifted 3 h and 6 h earlier. In all cases, the correlation with wind (Fig. 9) is notably weaker than correlation with discharge (Figs. 5–8), but the weak correlations describe coherent patterns in plume response to wind forcing.

On days with stronger upcoast winds, turbidity is higher in a zone extending upcoast from the mouth of the Russian River (Fig. 9, left panels). Evidently, this response to wind forcing takes time as the 3-hr and 6-hr lagged results show higher correlations and a better-defined plume zone. For zero lag, there is no response south of the mouth, but this is not the case for 3-hr and 6-hr lags, with significant correlations on the north side of Bodega Head, within Bodega Bay and around Point Reyes (likely explained by other turbid waters being advected northward during these upcoast, downwelling favorable winds). In contrast, turbidity increases south of the mouth on days with stronger downcoast winds, forming a 42-km-long continuous zone from the mouth of the river to Point Reyes (Fig. 9 second column), becoming more marked with 6-hr lag due to stronger negative correlations offshore. Correlations

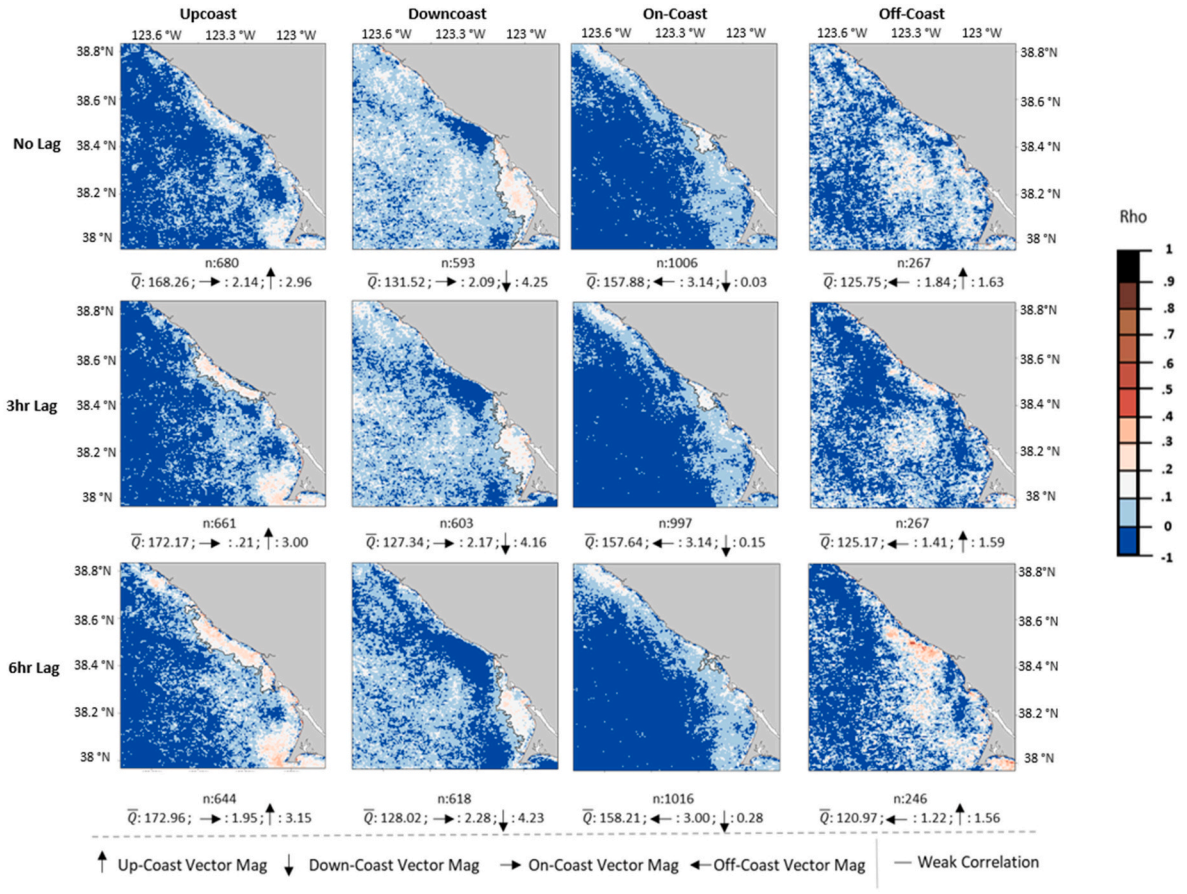

Fig. 9. Pixelwise correlation coefficients between Rrs_{645} and coincident daily average wind speed calculated separately for different wind quadrants (columns) and time lags (rows). The number of images in each subset (n) is listed beneath each image, along with information on average discharge (Q, m^3/s) and average windspeed (m/s) in alongshore and cross-shore orientations. Columns, left to right: daily average upcoast winds, downcoast winds, onshore winds, and offshore winds; Rows, top to down: no lag, 3 h lag, 6 h lag.

are low nearshore, specifically along the north coast of Point Reyes, which is persistently turbid due to wave-driven resuspension. During these NW winds, a marked zone of negative correlation is evident north of the mouth, indicating that turbid plume waters are less likely to be there with stronger downcoast winds, i.e., the upcoast plume pattern found on calm days and during upcoast winds is weakened or prevented by downcoast winds that are strong enough. Negative correlations west of Point Reyes similarly indicate that NW winds preclude upcoast propagation of turbid waters from the Gulf of Farallones. These results are all for periods when there is significant discharge from the Russian River (average Q ~ 130 m^3/s), which is not typical of the summer upwelling season.

Onshore winds also have a direct effect on turbidity, with higher turbidity observed near the river mouth with stronger onshore winds (Fig. 9 third column). This zone is centered on the mouth and strongest at the mouth. Correlations weaken with lag, indicating that the response to onshore winds is quicker than the response to alongshore winds. There is little correlation of turbidity with offshore winds at zero lag (Fig. 9 right panels). However, there is a marked nearshore zone extending north from the river mouth for images lagged 6 h, representing increased turbidity in the upcoast plume zone with increased offshore winds, which may represent a surface Ekman response. There is a similar zone of increased turbidity in the Gulf of Farallones, south of Point Reyes (i.e., just north of the mouth of San Francisco Bay).

3.5. Tidal effects

To explore tidal effects on the turbid plume of the Russian River, we calculate correlations between tidally varying water level (WL) and the turbidity index Rrs_{645} for each pixel (Fig. 10), as before, only using data when $p < 41$. Positive correlations indicate increased turbidity at higher tides and negative correlations indicate increased turbidity at lower tides. Correlations are weak, but small-scale zones are evident adjacent to the Russian River mouth.

Coherent zones of tide-correlated turbidity are most apparent for moderate discharge. For both the second and third discharge quartiles, there is a tendency for higher turbidity at high tide along the shore north of the mouth. However, to the south of the mouth, there is a tendency for higher turbidity at low tide (or lower turbidity at high tide), most apparent in high-discharge quartile plots. Also, for the second quartile, there is a small, elongated zone immediately off the mouth, corresponding to high turbidity at low tide.

4. Discussion

Runoff of freshwater from the land forms distinct low-salinity, turbid plumes in the coastal ocean, with shape and extent varying in response to river flow rate and ocean conditions. Prior work has identified at least four types of river plume, including classical large plumes controlled by a balance between buoyancy and Coriolis (Garvine, 1987; Horner-Devine, 2014), wind deflected plumes (Hickey et al., 2005; Lentz and Largier, 2006; Basdurak and Largier, 2022), tidally advected plumes (Basdurak et al., 2020), and plumes entrained into the surf zone by wave action (Kim et al., 2004; Clarke et al., 2007; Rodriguez et al., 2018; Kastner et al., 2019). Here we address a river where all these plume paradigms are observed, with different plume behavior occurring at

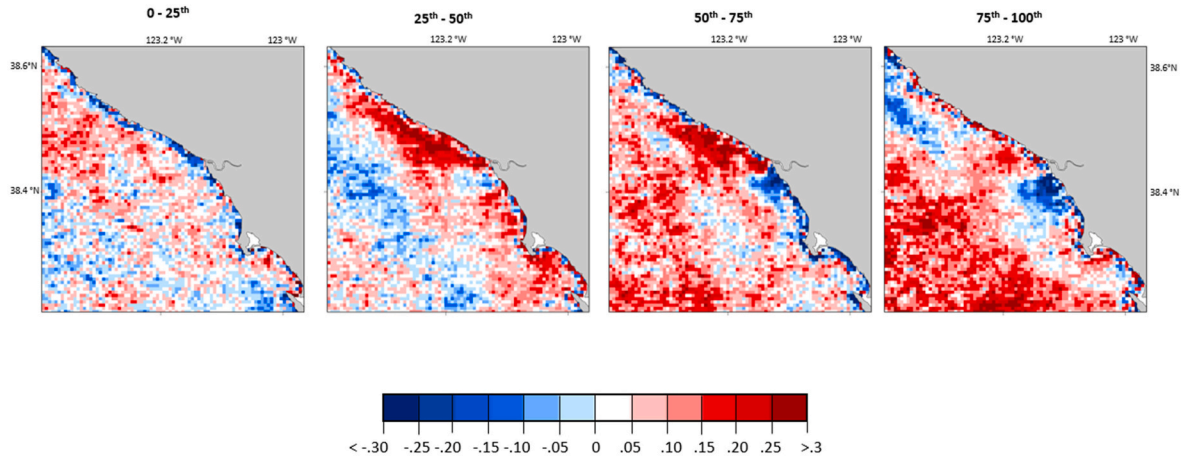

Fig. 10. Pixelwise correlation coefficients between Rrs_{645} and coincident water level (WL), calculated separately for four discharge quartiles. Maps are organized by increasing discharge (Q) quartiles from left to right: 0–25th percentile (16–42 m^3/s); 25th-50th percentile (42–84 m^3/s); 50th-75th (84–203 m^3/s); 75th - 100th percentile (203–2366 m^3/s).

different times. Outflow from the Russian River creates a turbid plume that is visible in satellite imagery (Fig. 1), both during high discharge and low discharge. Analysis of how turbidity at specific coastal ocean locations varies with changes in discharge, wind, waves, and tides reveals coherent patterns that reflect the influence of all four factors. While satellite data only enable us to track turbidity (concentration of fine suspended sediment), it is used here as a tracer for salinity patterns and patterns in the concentration of runoff-borne material.

Satellite data are only from the surface of the plume, lacking information on stratification and sub-surface structure. However, our results corroborate models and experiments, which help us explain the observed plume surface patterns. This study is novel in the degree of replication (~1500 whole-plume observations over 15 years), which allows us to consider multiple interacting drivers rather than reducing our analysis to a single dynamic. This immense data set shows the complexity and variability in plume types (different dominant forcing) – and variability even within plume types due to secondary forcing terms. Results show coherent patterns that vary with changes in river discharge, wind speed and direction, tidal phase, and wave height.

4.1. River discharge

The strongest control on plume size and shape is exerted by the river outflow rate (discharge Q), shown by pixelwise correlation with turbidity (Figs. 5–8). Not only does high discharge result in a large volume of water, but it also represents a high buoyancy flux that explains spreading of the plume beyond the near field (where inertia dominates). The larger spatial scales (offshore extent, plume area) result in stronger Coriolis forcing and the observed tendency for high-discharge plumes to turn to the right, i.e., upcoast (Fig. 6). Thus, the Russian River plume behaves like other "large" river plumes in the classical dichotomy articulated by Garvine (1995) and others (Horner-Devine et al., 2015). However, while the Coriolis-induced turning region is observed, discharge from the Russian River and other SMRS is highly variable and high-discharge conditions last for only a few days so that one does not expect a coastal buoyancy current to form as observed for systems with more persistent outflow, e.g., Chesapeake Bay (Rennie et al., 1999), Mississippi River (Castillo and Miller, 2008). In contrast to the coasts characterized by singular, large outflows, the northern California coast is characterized by multiple SMRS that experience simultaneous high discharge events. When plumes coalesce (Warrick and Farnsworth, 2017) a coastal buoyancy current may form, as observed off Oregon by Mazzini et al. (2014). For weaker discharges, Coriolis is not a primary forcing term, and the "small" plume configuration is shaped primarily by wind and tide as seen in models (Basdurak et al., 2020; Basdurak and Largier, 2022).

4.2. Wind speed and direction

The coastal ocean off northern California is subject to northerly upwelling-favorable winds for much of the year (Garcia-Reyes and Largier, 2012), but winds are more variable in winter when runoff events occur. The plume pattern is markedly different between days with upcoast (downwelling favorable) and downcoast (upwelling favorable) winds (Figs. 8 and 9). In all wind states the correlation between turbidity and discharge remains moderately strong near the mouth of the river (Fig. 8), but extends only upcoast during southerly/upcoast winds, and downcoast during northerly/downcoast winds. This indicates that wind forcing overcomes the buoyancy-Coriolis balance that makes the plume turn right and extend upcoast in the absence of wind (Fig. 7). This response of the plume to wind is also seen in the pixelwise correlation between turbidity and wind speed, calculated for different wind states (Fig. 9). While turbidity-wind correlations are notably weaker than turbidity-discharge correlations, during upcoast winds there is a coherent zone north of the mouth where higher turbidities are observed during stronger winds (most apparent with lag between turbidity and wind), i.e., it is not just the wind direction but also the strength of the wind that influences plume behavior. Likewise, a coherent zone is observed south of the mouth during downcoast winds.

One would expect turbidity-wind correlations to be weaker than turbidity-discharge correlations as wind does not alter the amount of runoff or turbidity and only influences the flow patterns in the receiving coastal waters. As discussed by Basdurak and Largier (2022), wind has multiple effects on river plumes including the direct effect of wind stress and the effect of wind-driven currents. Alongshore currents in this region are well correlated with alongshore wind forcing (Winant et al., 1987; Largier et al., 1993) and these currents can push and drag plume waters by upstream frontal convergence and underlying interfacial stress, respectively. The increase in correlation with lag is consistent with the lag in correlations between alongshore current and wind. At the same time, surface wind stress can force the plume directly, and most effectively when plume stratification is strong enough to contain added momentum in the shallow surface plume layer. Basdurak and Largier (2022) show that surface stress may move the whole plume, when mixing extends throughout the plume layer, or it may strain the plume and thus thin it and spread it downwind, when mixing decreases with depth (suppressed by stratification in the plume). These surface data provide no direct insight to sub-surface structure, but it is notable in Fig. 9 that the zone of coherent turbidity-wind correlation is confined nearshore with downwelling winds (onshore Ekman transport) and

spread offshore with upwelling winds (offshore Ekman transport).

We find that cross-shore winds are also important, consistent with model results from Basdurak and Largier (2022). Indeed, turbidity-discharge correlations are strongest close to the river mouth during onshore winds (Fig. 8), indicating that high-turbidity waters are retained near the mouth during onshore winds, countering the offshore forcing due to outflow inertia and buoyancy-driven spreading. As onshore winds are not expected to drive strong onshore currents, this effect is likely due to direct wind forcing, i.e., surface wind stress. While there is a coastwide narrowing in the band of turbidity-discharge correlations with onshore winds, the zone of moderate/strong correlation extends only ~10 km alongshore (both upcoast and downcoast), indicating that onshore winds tend to prevent upcoast propagation of the plume. A similar near-mouth zone is observed for turbidity-wind correlation, showing that turbidities are higher with stronger onshore winds (although not nearshore downcoast of the mouth). It is interesting to note that the turbidity response to onshore wind does not exhibit a lag, which is consistent with direct forcing by wind stress and shorter time scales that do not involve Coriolis forcing. This plume compression by onshore winds has received little prior attention and only in models (Osadchiev et al., 2013; Basdurak and Largier, 2022) – we are unaware of any prior observations showing this effect.

4.3. Waves

As shown by Rodriguez et al. (2018) and Kastner et al. (2019), waves can stall the outflow jet and trap runoff and thus turbidity in surf zone and rip-current influenced nearshore waters. Here, we show that wave forcing can also be important for larger rivers, such as the Russian River – either during low discharge or during periods of large waves and high radiation stress. Through analysis of turbidity-discharge correlations, we quantify a threshold for the wave-outflow parameter p formulated by Rodriguez et al. (2018): for p values in the upper six deciles, we do not see plume-level Rrs_{645} turbidity at pixels located 1 km offshore of the mouth of the Russian River, so we choose $p = 41$ as the threshold for plumes escaping wave-dominated nearshore waters. This is comparable with a p-value of 20 obtained by Rodriguez et al. (2018) from numerical simulations representing conditions at the mouth of Tijuana River (H_s = 1m; Q = 10 m/s^3). During strong wave forcing, turbid outflow can be trapped nearshore for river discharge as high as ~40 m^3/s, showing that wave forcing is likely to be important for all SMRS on wave-exposed coasts. This study is the first empirical validation of this wave-outflow momentum balance for a SMRS.

While river waters may be exported from the surf zone through rip currents after being initially trapped (Clarke et al., 2007), the inertia of the outflow has been lost and even the buoyancy head has been dissipated by mixing in the nearshore. Consequently, these turbid, low-salinity waters are more likely to be dispersed passively and without stratification. And without immediate mechanisms to transport these waters offshore, they are likely to remain in contact with the shore far from the mouth of the river (e.g., Kim et al., 2004).

4.4. Tides

Through an analysis of turbidity-waterlevel correlations (Fig. 10), we show tidal variability in plume behavior addition to strong control by discharge and additional significant control by wind forcing. Basdurak et al. (2020) model the influence of tide on outflow from an idealized SMRS in California and show the alongshore advection of the plume by reversing tidal currents (best described by comparison to the wagging tail of a dog). As noted by Basdurak and Largier (2022), these tidal influences are readily dominated by wind forcing, but in all but the strongest winds the plume continues to exhibit some tidal variability. Consistent with Basdurak et al. (2020) we observed increasing turbidity north of the river mouth during rising tides (Fig. 10), explained by the northward advection of turbid outflow by alongshore tidal currents. The effect is not observed for weak discharge when turbidity is low and the plume can easily be deflected by winds. The effect is strongest for moderately high discharge (up to ~200 m^3/s), when turbidity is higher and there is a tendency for upcoast transport, which can be enhanced by upcoast tidal currents. For highest discharges, correlations are low as the plume is persistent along this coast, without turbidity gradients that can be advected by tidal currents.

South of the river mouth (downcoast), turbidity increases over the falling tide (Fig. 10), consistent with southward advection of turbid waters by the alongshore tidal current. Even if the tidal component is smaller than wind-driven component, it introduces tidal variability in the current which will explain tidal variability in turbidity at a point, given the alongshore gradient in turbidity. Again, the effect is not observed for weakest discharges, but here it is strongest for the upper two discharge quartiles and higher correlations are observed than upcoast of the mouth.

In addition to this alongshore tidal advection, tides modulate the outflow from the Russian River estuary (Behrens et al., 2013). This effect may explain the offshore elongated shape of the negative correlation observed for the second discharge quartile (Fig. 10), which is included in the negative correlation zone for third and fourth quartiles. Tidal fluctuations in outflow are more marked for weak/moderate river discharge when river flow can be retained in the estuary during rising tides and maximum outflow of turbid waters occurs during falling tides, explaining offshore advection and tidally increased turbidity in this zone. Downcoast of the mouth the tidal efflux effect and the alongshore tidal advection effect both account for a negative correlation, whereas the effects have opposite sign upcoast of the mouth, which may explain the marked negative zone immediately south of the mouth of the river. This may also explain the absence of a positive signal about the inlet in the lowest discharge quartile in Fig. 10, as a rising tide could reduce outflow from small discharges.

4.5. Other nearby sources of turbidity

There are multiple sources of turbidity in the coastal waters off northern California, including land runoff, bay outflow, wave-driven resuspension, and tidal resuspension. Tidal resuspension is not apparent in open waters outside of tidal bays like San Francisco Bay, but wave-driven resuspension of fine sediment is evident in nearshore waters along the coast of northern California, which is the focus of a companion study (Speiser et al. in prep.) – this is evident as high mean turbidity along the wave-exposed north shores of Bodega Head and Point Reyes (Fig. 4). Here our interest is in the effect of river plumes, which we explore through the Russian River case study. Patterns of turbidity-discharge correlation show a clear maximum close to the river mouth, weakening with distance away from the mouth due to decreasing turbidity and the importance of other processes and sources. Some alternative turbidity sources are evident in our study because discharge from nearby rivers (e.g., Gualala River) is correlated with that in the Russian River, thus accounting for the high turbidity-correlation values off the mouth of the Gualala River (38.77° N, Figs. 5, 7 and 8). The Gualala plume is visible on February 28, 2019 (Fig. 1b) and in a map of mean turbidity (Fig. 4).

High levels of turbidity in Bodega Bay and Tomales Bay, evident in the image from February 28, 2019 (Fig. 1C), are also associated with land runoff through smaller rivers including Estero Americano and Estero San Antonio that enter Bodega Bay and Walker Creek and Lagunitas Creek that enter Tomales Bay. Again, high discharge events occur simultaneously in these small rivers and the Russian River following rain events, thus accounting for high turbidity-discharge correlations in Bodega Bay (Figs. 5–7), which can merge with high correlations associated with the Russian River (Fig. 8) – and potentially misinterpreted as being due to the Russian River.

A third regional source of turbidity is outflow from San Francisco Bay, entering the ocean through its mouth south of Point Reyes

(37.8°N). Although turbidity is lower than in river plumes (Fig. 1C), there is a coherent pattern of turbidity associated with northward transport past Point Reyes (Kaplan and Largier, 2006; Largier, 2020) that is evident during high-discharge events when the Bay outflow turns right under the influence of Coriolis forcing (Fig. 6) and that accounts for notably high turbidity-discharge correlations during southerly winds (Fig. 8) and markedly higher turbidities during stronger southerly winds (Fig. 9). These low-salinity events are recorded at Bodega Head (Largier, 2020; Ricart et al., in review).

4.6. Implications of plume patterns

Satellite data on surface reflectance allows analysis of surface turbidity patterns that we have quantified and subsequently explained in terms of plume behavior. The analysis of turbidity is immediately valuable in providing insight to sub-surface light levels important for photosynthesis and insight to the fate of fine terrigenous sediment and sorbed materials that can include organics, metals, and pollutants. Further, the spatial extent (>30 km) and temporal persistence (>1 day) of the observed turbidity patterns indicate slow settling velocities so that the decrease in concentration away from the mouth of the river is likely controlled by mixing and dilution. In that case these patterns of turbidity are also a reasonable first estimate of patterns of dissolved material including salinity, nutrients, and carbon. The zone of impact (area where river-borne material is concentrated) varies with changes in discharge, winds, waves, and tides – but clear correlations emerge that can explain patterns of exposure to diverse river-borne constituents. There is growing interest in the exposure of shoreline environments (e.g., recreational beaches) and nearshore environments (e.g., kelp forests) to runoff, which may transport pathogens, e.g., toxoplasma gondii (Shapiro et al., 2015) and fecal coliform (Kim et al., 2004) and other pollutants (Rogowski et al., 2015). There is also growing interest in the role of river plumes in explaining kelp refugia amidst a catastrophic loss of kelp forests off northern California (Rogers-Bennett et al., 2019; Cavanaugh et al., 2023; Ricart et al., in review), in their potential role in ameliorating or exacerbating nearshore ocean acidification due to their high carbon content (Stets et al., 2017), and in their potential for explaining localized stratification and hypoxia. Shoreline attachment is shown to be strongest on the upcoast side of the Russian River mouth and this is generally expected. Stronger upwelling winds are anticipated with climate change (García-Reyes et al., 2023) and that would reduce this effect, but at the same time more intense flow events are anticipated with more frequent atmospheric river events (Albano et al., 2020) and that would intensify the shoreline impacts upcoast of the mouth.

5. Conclusion

The long record of daily MODIS Aqua imagery of coastal waters off the Russian River offers a comprehensive overview of plume behavior, specifically identifying features characteristic of plumes formed off the mouth of Mediterranean-climate, small-mountainous-river-systems (SMRS). This expansive dataset, contextualized by coincident environmental monitoring data, corroborates several plume models and offers new insights into the interaction between buoyancy-Coriolis forcing with wind forcing, wave forcing, and tidal forcing.

Results from our study highlight the significant control of river outflow rate on plume size and shape and the contrast between small and large plumes. High discharge rates result in “large” plumes with significant Coriolis influence beyond the near field whereas low discharge rates result in “small” plumes subject to forcing by winds and tides. The spatial extent of the plume varies significantly, with the average alongshore extent of turbid plumes increasing from 14 km for the lowest discharge quintile to 77 km in the highest quintile. Similarly, the offshore extent increases from 3 km to 14 km across the same quintiles, and plume area increases from 20 km^2 to 698 km^2. In the highest quintile, outflow from the Russian River plumes coalesces with other regional outflows, obscuring the degree of individual contribution to coastal turbidity that extends throughout the study site.

Maps of the correlation of turbidity with observed environmental indices clarify the roles of wave, tide, and wind forcing. Wave forcing, quantified through the wave-outflow momentum balance parameter p, shows that plume-level turbidity is not observed beyond 1 km offshore when $p > 41$, as wave radiation stress dominates river outflow momentum. For plumes with enough discharge momentum to overcome wave forcing, near-field dispersion is modulated by tidal forces, causing upcoast and downcoast deflection during rising and falling tides, respectively. The far-field plume is strongly controlled by wind direction, with discharge-correlated turbidity extending more than 30 km upcoast (and minimal downcoast signal) during southerly winds. During northerly winds, discharge-correlated turbidity extends 30 km downcoast with no upcoast signal. This demonstrates the dominance of wind over Coriolis forcing, except during weak winds or very high discharge. Onshore winds compress river sediment turbidity towards the shore.

Our analysis was limited to observing single-feature correlations and used multi-feature data subsetting to examine combined effects, rather than employing computationally expensive multivariate statistics. These limitations highlight the need for further studies using advancing computational techniques and higher-resolution datasets. Advanced techniques, particularly in machine learning and computer vision processing of high-resolution imagery, will help capture the fine, dynamic details needed to understand the controls on smaller outflows from SMRS. We are motivated by ever-growing high-resolution imagery datasets and developing capabilities in machine learning to continue research in these essential nearshore freshwater outflow processes. Nevertheless, these observations are invaluable in revealing the complexity of space-time patterns in land runoff and in ground-truthing recent numerical models. Our analysis of an immense number of plume visualizations under diverse discharge, wind, wave, and tide conditions provides novel insights that can guide future model and field experiments.

CRediT authorship contribution statement

William H. Speiser: Writing – original draft, Visualization, Validation, Methodology, Investigation, Formal analysis, Data curation, Conceptualization. **John L. Largier:** Writing – review & editing, Investigation, Funding acquisition, Conceptualization.

Declaration of competing interest

The authors declare that they have no known competing financial interests or personal relationships that could have appeared to influence the work reported in this paper.

Data availability

Data will be made available on request.

Acknowledgments

We are grateful for funding from the State of California (CA Ocean Protection Council grant) and the National Science Foundation (DISES Grant #2108002) and Sonoma Water.

References

Albano, C.M., Dettinger, M.D., Harpold, A.A., 2020. Patterns and drivers of atmospheric river precipitation and hydrologic impacts across the western United States. J. Hydrometeorol. 21 (1), 143–159.

Armi, L., Farmer, D.M., 1986. Maximal two-layer exchange through a contraction with barotropic net flow. J. Fluid Mech. 164, 27–51.

Aurin, D., Mannino, A., Franz, B., 2013. Spatially resolving ocean color and sediment dispersion in river plumes, coastal systems, and continental shelf waters. Remote Sens. Environ. 137, 212–225.
Basdurak, N.B., Largier, J.L., 2022. Wind effects on small-scale river and creek plumes. J. Geophys. Res.: Oceans 128, e2021JC018381.
Basdurak, N.B., Largier, J.L., Nidzieko, N.J., 2020. Modeling the dynamics of small-scale river and creek plumes in tidal waters. J. Geophys. Res.: Oceans 125 (7), e2019JC015737.
Behrens, D.K., Bombardelli, F.A., Largier, J.L., Twohy, E., 2013. Episodic closure of the tidal inlet at the mouth of the Russian River—a small bar-built estuary in California. Geomorphology 189, 66–80.
Cavanaugh, K.C., Cavanaugh, K.C., Pawlak, C.C., Bell, T.W., Saccomanno, V.R., 2023. CubeSats show persistence of bull kelp refugia amidst a regional collapse in California. Remote Sens. Environ. 290, 113521.
Del Castillo, C.E., Miller, R.L., 2008. On the use of ocean color remote sensing to measure the transport of dissolved organic carbon by the Mississippi River Plume. Remote Sens. Environ. 112 (3), 836–844.
Fernández-Nóvoa, D., Mendes, R.D., Decastro, M., Dias, J.M., Sánchez-Arcilla, A., Gómez-Gesteira, M., 2015. Analysis of the influence of river discharge and wind on the Ebro turbid plume using MODIS-Aqua and MODIS-Terra data. J. Mar. Syst. 142, 40–46.
Fong, D.A., Geyer, W.R., 2001. Response of a river plume during an upwelling favorable wind event. J. Geophys. Res.: Oceans 106 (C1), 1067–1084.
Fong, D.A., Geyer, W.R., 2002. The alongshore transport of freshwater in a surface-trapped river plume. J. Phys. Oceanogr. 32 (3), 957–972.
García-Reyes, M., Koval, G., Sydeman, W.J., Palacios, D., Bedriñana-Romano, L., DeForest, K., Hines, E., 2023. Most eastern boundary upwelling regions represent thermal refugia in the age of climate change. Front. Marine Sci. 10, 1158472.
Garvine, R.W., 1995. A dynamical system for classifying buoyant coastal discharges. Continent. Shelf Res. 15 (13), 1585–1596.
Gerbi, G.P., Chant, R.J., Wilkin, J.L., 2013. Breaking surface wave effects on river plume dynamics during upwelling-favorable winds. J. Phys. Oceanogr. 43 (9), 1959–1980.
Geyer, W.R., Hill, P., Milligan, T., Traykovski, P., 2000. The structure of the Eel River plume during floods. Continent. Shelf Res. 20 (16), 2067–2093.
Griggs, G.B., Hein, J.R., 1980. Sources, dispersal, and clay mineral composition of fine-grained sediment off central and northern California. J. Geol. 88 (5), 541–566.
Hetland, R.D., 2010. The effects of mixing and spreading on density in near-field river plumes. Dynam. Atmos. Oceans 49 (1), 37–53.
Hickey, B.M.S.L., Geier, S., Kachel, N., MacFadyen, A., 2005. A bi-directional river plume: the Columbia in summer. Continent. Shelf Res. 25 (14), 1631–1656.
Horner-Devine, A.R., Jay, D.A., Orton, P.M., Spahn, E.Y., 2009. A conceptual model of the strongly tidal Columbia River plume. J. Mar. Syst. 78 (3), 460–475.
Horner-Devine, A.R., Hetland, R.D., MacDonald, D.G., 2015. Mixing and transport in coastal river plumes. Annu. Rev. Fluid Mech. 47, 569–594.
Kastner, S.E., Horner-Devine, A.R., Thomson, J.M., 2019. A conceptual model of a river plume in the surf zone. J. Geophys. Res.: Oceans 124 (11), 8060–8078.
Kaplan, D.M., Largier, J., 2006. HF radar-derived origin and destination of surface waters off Bodega Bay, California. Deep Sea Res. Part II Top. Stud. Oceanogr. 53 (25–26), 2906–2930.
Kim, J.H., Grant, S.B., McGee, C.D., Sanders, B.F., Largier, J.L., 2004. Locating sources of surf zone pollution: a mass budget analysis of fecal indicator bacteria at huntington beach, California *environmental science & technology*, 38, 2626–2636. https://doi.org/10.1021/es034831r.
Largier, J.L., Magnell, B.A., Winant, C.D., 1993. Subtidal circulation over the northern California shelf. J. Geophys. Res.: Oceans 98 (C10), 18147–18179.
Largier, J.L., 2020. Wind-modulated buoyancy current pulses associated with outflow from San Francisco bay. In: Ocean Sciences Meeting 2020. AGU.
Largier, J., Behrens, D., Hewett, K., Koohafkan, M., Robart, M., Dann, D., Roettger, R., 2020. Managing the mouth of the Russian River estuary, California. In: Slinger, J., Taljaard, S., dHont, F. (Eds.), Complex Coastal Systems – Transdisciplinary Learning on International Case Studies. Delft Academic Press, pp. 71–86.
Lentz, S.J., Largier, J., 2006. The influence of wind forcing on the Chesapeake Bay buoyant coastal current. J. Phys. Oceanogr. 36 (7), 1305–1316.
Mazzini, P.L., Barth, J.A., Shearman, R.K., Erofeev, A., 2014. Buoyancy-driven coastal currents off Oregon during fall and winter. J. Phys. Oceanogr. 44 (11), 2854–2876.
Mendes, R., Vaz, N., Fernández-Nóvoa, D., Da Silva, J.C.B., Decastro, M., Gómez-Gesteira, M., Dias, J.M., 2014. Observation of a turbid plume using MODIS imagery: the case of Douro estuary (Portugal). Rem. Sens. Environ. 154, 127–138.
Miche, M., 1944. Mouvements ondulatoires de la mer en profondeur constante ou décroissante. Annales de Ponts et Chaussées 1944 (3), 369–406 (1) 26-78,(2) 270-292.
O'Reilly, W.C., Olfe, C.B., Thomas, J., Seymour, R.J., Guza, R.T., 2016. The California coastal wave monitoring and prediction system. Coast Eng. 116, 118–132.
Pullen, J., Allen, J.S., 2001. Modeling studies of the coastal circulation off northern California: statistics and patterns of wintertime flow. J. Geophys. Res.: Oceans 106 (C11), 26959–26984.
Rennie, Sarah E., Largier, John L., Lentz, Steven J., 1999. Observations of a pulsed buoyancy current downstream of Chesapeake Bay. J. Geophys. Res.: Oceans 104 (C8), 18227–18240.
Ricart, A.M., Gómez, G.B., Karm, R.H., Largier, J.L., Souza, V., Dias, A.S., Velázquez, M. G., Nelson, T., Cavanaugh, K.C., Cavanaugh, K.C., Hughes, B.B., in review. Persistent kelp forests during a massive decline reveal the importance of land-sea connectivity. Ecology. submitted for publication.
Rodriguez, A.R., Giddings, S.N., Kumar, N., 2018. Impacts of nearshore wave-current interaction on transport and mixing of small-scale buoyant plumes. Geophys. Res. Lett. 45 (16), 8379–8389.
Rogers-Bennett, L., Catton, C.A., 2019. Marine heat wave and multiple stressors tip bull kelp forest to sea urchin barrens. Sci. Rep. 9 (1), 15050.
Rogowski, P.A., Terrill, E., Schiff, K., Kim, S.Y., 2015. An assessment of the transport of southern California stormwater ocean discharges. Mar. Pollut. Bull. 90 (1–2), 135–142.
Runyan, K., Griggs, G.B., 2003. The effects of armoring seacliffs on the natural sand supply to the beaches of California. J. Coast Res. 336–347.
Saldías, G.S., Sobarzo, M., Largier, J., Moffat, C., Letelier, R., 2012. Seasonal variability of turbid river plumes off central Chile based on high-resolution MODIS imagery. Remote Sens. Environ. 123, 220–233.
Saldías, G.S., Largier, J.L., Mendes, R., Pérez-Santos, I., Vargas, C.A., Sobarzo, M., 2016. Satellite-measured interannual variability of turbid river plumes off central-southern Chile: spatial patterns and the influence of climate variability. Prog. Oceanogr. 146, 212–222.
Shapiro, K., VanWormer, E., Aguilar, B., Conrad, P.A., 2015. Surveillance for Toxoplasma gondii in California mussels (*Mytilus californianus*) reveals transmission of atypical genotypes from land to sea. Environ. Microbiol. 17 (11), 4177–4188.
Stets, E.G., Butman, D., McDonald, C.P., Stackpoole, S.M., DeGrandpre, M.D., Striegl, R. G., 2017. Carbonate buffering and metabolic controls on carbon dioxide in rivers. Global Biogeochem. Cycles 31 (4), 663–677.
Thomson, J., Horner-Devine, A.R., Zippel, S., Rusch, C., Geyer, W., 2014. Wave breaking turbulence at the offshore front of the Columbia River plume. Geophys. Res. Lett. 41 (24), 8987–8993.
Wang, M., Son, S., Shi, W., 2009. Evaluation of MODIS SWIR and NIR-SWIR atmospheric correction algorithms using SeaBASS data. Remote Sens. Environ. 113 (3), 635–644.
Warrick, J.A., DiGiacomo, P.M., Weisberg, S.B., Nezlin, N.P., Mengel, M., Jones, B.H., et al., 2007. River plume patterns and dynamics within the Southern California Bight. Continent. Shelf Res. 27 (19), 2427–2448.
Warrick, J.A., 2020. Littoral sediment from rivers: patterns, rates and processes of river mouth morphodynamics. Front. Earth Sci. 8, 355.
Warrick, J.A., Farnsworth, K.L., 2017. Coastal river plumes: collisions and coalescence. Prog. Oceanogr. 151, 245–260.
Wheatcroft, R.A., Goñ i, M.A., Hatten, J.A., Pasternack, G.B., Warrick, J.A., 2010. The role of effective discharge in the ocean delivery of particulate organic carbon by small, mountainous river systems. Limnol. Oceanogr. 55 (1), 161–171.
Winter, S.A., 2020. A investigation of the closure regimes of California's bar-built estuaries. MS Thesis 92. UC Davis.
Wong, S.H., Monismith, S.G., Boehm, A.B., 2013. Simple estimate of entrainment rate of pollutants from a coastal discharge into the surf zone. Environ. Sci. Technol. 47 (20), 11554–11561.